Electronic supplement to the paper "Immersed granular collapse: From viscous to free-fall unsteady granular flows"

Laurent Lacaze[1], Joris Bouteloup[1], Benjamin Fry[1], and Edouard Izard[1],

[1]Institut de Mécanique des Fluides de Toulouse (IMFT), Université de Toulouse, CNRS, INPT, UPS, Toulouse, France

(Received xx; revised xx; accepted xx)

The objective of this electronic supplement is to show the relevance of the closure models used in the meso-scale numerical approach by mean of a so-called microscole approach. It will also be shown that microscale approaches should fail to provide a full description of the dynamics at all scales for immersed granular flow due to uncertainty of the local influence of surface roughness on short-range particle interactions. This is discussed here in term of a numerical regularization length of the interface between a solid grain and the fluid phase by mean of a smooth weight function. This parameterized regularization length affects fluid dissipation during collapse leading to an impact on the effective drag and the effective viscosity at the mesoscale. However, results show to be relevant with models from the literature and not to play a major role on the final deposit. Moreover, as discussed in the main manuscript, the origin of the influence of fluid dissipation can be simply understood and then accounting for through the definition of the relevant dimensionless numbers (see main manuscript). Finally, a third order correction to the Batchelor viscosity for dense suspension is proposed. The numerical value of this correction, as given in the main manuscript, is a fit of the data obtained from the numerical simulations at the microscale. Using these closure models at the mesosclae, the mesoscale simulations (VANS/DEM) are compared with the microscale simulations (IBM/DEM).

1. Microscale model: IBM/DEM

1.1. *Numerical method*

First of all, a brief description of the IBM approach used as the microscale description is given. Details of the method have been given in Izard *et al.* (2014) and tested on a configuration similar to the one studied in the present contribution (Izard *et al.* 2018). The fluid phase is solved using an Immersed Boundary Method, allowing to model the fluid dynamics at a spatial scale smaller than the particle (Bigot *et al.* 2014; Pierson & Magnaudet 2018). Briefly, the IBM forcing used here is a volume force added to the Navier-Stokes equations for the fluid phase which is only imposed on the part of the meshgrid within the volume of the particle to ensure the velocity at these points to be the local velocity of the solid body. The Navier-Stokes equations for an incompressible viscous fluid of constant density ρ and viscosity η are thus resolved on the entire spatial domain including the particles, reading

$$\nabla.\mathbf{u} = 0, \tag{1.1}$$

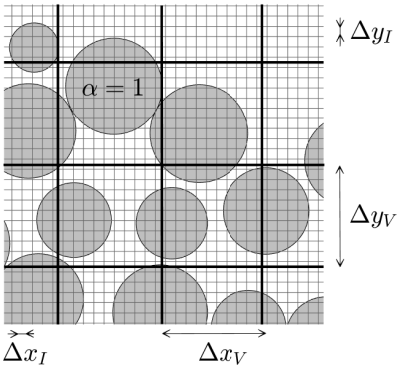

FIGURE 1. Sketch of the spatial scales used for the IBM/DEM approach in a 2D (x, y) cross-section (thin lines). Also shown, the meshgrid used in VANS/DEM simulations for comparison with the IBM/DEM simulations (thick lines).

$$\frac{D\mathbf{u}}{Dt} = \mathbf{g} - \frac{1}{\rho}\nabla p + \frac{1}{\rho}\nabla \cdot \left[\eta \left(\nabla \mathbf{u} + {}^t\nabla \mathbf{u}\right)\right] + \frac{1}{\rho}\mathbf{f}_j^{ibm} \quad j \in [1, N_p], \tag{1.2}$$

with $\mathbf{u}$ the fluid velocity, p the fluid pressure and $D/Dt = \partial/\partial t + \mathbf{u}\cdot\nabla$. These equations are solved on a regular spatial meshgrid, $\Delta x_I = \Delta y_I = \Delta z_I < d$ which is considered as the resolved scale for the fluid phase in the present study (see figure 2(a) for a sketch). In practice, the IBM force $\mathbf{f}_j^{ibm}$ of each particle $j \in [1, N_p]$ at a position $\mathbf{x}_j$ (position of its centre of mass) is written as

$$\mathbf{f}_j^{ibm} = \alpha(\mathbf{x} - \mathbf{x}_j)\rho\frac{\mathbf{v}_j + \mathbf{r} \times \omega_j - \mathbf{u}}{\Delta t_f}, \tag{1.3}$$

which is a force per unit volume and with Δt_f the time-step used for time advancement in the numerical resolution of the fluid phase. Here α is a continuous function being 1 in the particle and 0 outside, with a transition region from the interior of the particle to the outer region of about one-to-three grid cells at the interface between the particle and the fluid (see for instance Yuki *et al.* 2007; Pierson & Magnaudet 2018, and figure 2 for a 2D sketch). The shape of the function used will be discussed in the following section.

To finish with, integrating (1.2) over the volume $\mathcal{V}_j$ of each particle j, leads to the expression of $\mathbf{F}_j^h$ and Γ_j^h to be included in the DEM (see main paper). One obtains (Pierson & Magnaudet 2018)

$$\mathbf{F}_j^h = \rho\frac{D}{Dt}\int_{\mathcal{V}_j} \mathbf{u} dV - \int_{\mathcal{V}_j} \mathbf{f}_j^{ibm} dV - m_j^f \mathbf{g}, \tag{1.4}$$

$$\Gamma_j^h = \rho\frac{D}{Dt}\int_{\mathcal{V}_j} \mathbf{r} \times \mathbf{u} dV - \rho\int_{\mathcal{V}_j} \mathbf{r} \times \mathbf{f}_j^{ibm} dV, \tag{1.5}$$

with $m_j^f = \rho\mathcal{V}_j$ and $j \in [1, N_p]$.

1.2. *Limitation at the roughness nanoscale : an alternative strategy.*

In this paper, microscale referred to a scale smaller than the grain diameter at which the fluid is resolved, using here an IBM approach. However, this scale can hardly be as small as surface roughness of real grain, due to computational limitation. A full description

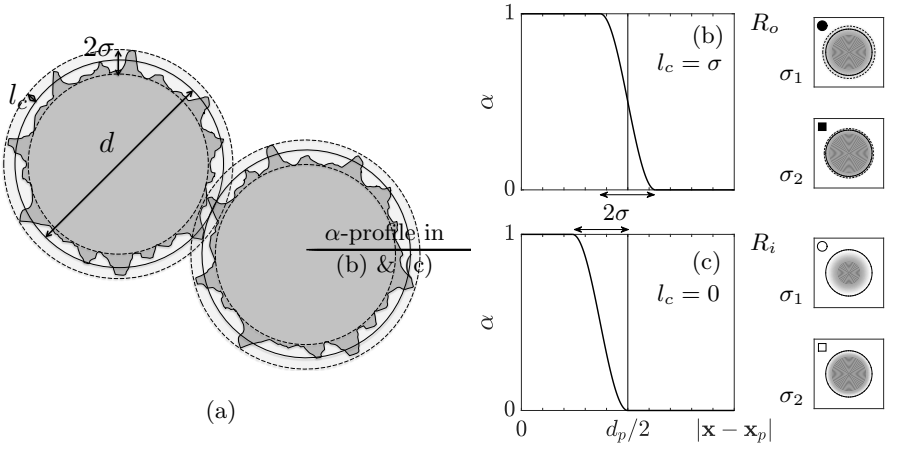

FIGURE 2. (a) Sketch of a typical rough grain in contact with another, and its effective length scales according to the description used here (see text for details). α-profiles of the IBM weight function along the radial direction of the grains for roughness-mimic configurations R_o (b) and R_i (c). Right column: vignettes sketching α contours within particles for the four couple (R, σ) together with their corresponding symbols used in figures 4 and 6.

at the scale of surface roughness would be of main interest but remains quite costly and lack physical and experimental knowledge for interpretation. The modelled grains thus remain spheres, as in the VANS/DEM as well as DEM for dry situations. This is a classical approach in the literature, but deserves a dedicated attention.

When solving the fluid flow around spherical objects close to contact, the limitation of the IBM approach has to be anticipated.

First, the scale of the grain roughness plays a major role on the mechanisms of grain interaction for both the interstitial fluid phase, particularly the interstitial lubrication force prior and after solid contact, and the solid contact properties. For the granular phase solved using the DEM approach, the grain is thus often modelled by a sphere and the influence of the roughness parameters is included into the friction parameter μ_p. For the fluid phase, assumptions are also required. As roughness is small for controlled laboratory grains, its influence on the fluid phase is usually discussed through a cut-off length of the lubrication force which dominates the dynamics of two near-contact particles.

Second, the numerical procedure of IBM also suffers its own small scale weakness when dealing with solid moving objects close to contact, which is the meshgrid size. In particular, two perfectly smooth objects close to contact could not be modelled, and the meshgrid provides a numerical cut-off length for the fluid phase (see for instance Ardekani 2008; Kempe & Fröhlich 2012). As this numerical length is often larger than the expected roughness length scale of solid particles used in laboratory experiments, a subscale lubrication model is often used in the literature to provide the fluid dissipation (see for instance Izard *et al.* 2014; Gallier *et al.* 2014). Again, the lubrication model requires a cut-off length at the expected roughness scale.

In order to continuously approach solid contact, we propose here an alternative approach. In the following, the IBM algorithm used is a direct forcing approach using a volume fraction α to define the boundary (see Yuki *et al.* 2007; Izard *et al.* 2014, and figure 2(b–c)). We thus make use of this numerical volume fraction to provide a description of the surface of the grain as a porous interface, with a local velocity of

the form $\alpha u_p + (1-\alpha)u_f$, with u_p and u_f a typical particle velocity and fluid velocity respectively. The weakness of this approach is that it only provides modelling of the roughness down to the meshgrid length scale which is of the order of 5%-d, but it prevents for any further subscale modelling. Accordingly, the roughness of particle is modelled using this approach as follows. A rough particle is characterized, among other, by a roughness length 2σ which described a typical scale of roughness height (see figure 2(a)). Depending on the roughness structure, solid contact can then occur at different distances from the particles centers. We choose here to identify this solid contact as an equivalent contact of two spherical particles of equivalent grain diameter, which is chosen here as the grain diameter d. Then, the interpenetration of roughness is labelled l_c (see figure 2(a) for a sketch of this equivalent contact parametrization). The volume fraction α of the IBM is thus defined accordingly, i.e. decreasing from 1 to 0 on the length scale 2σ (see figure 2(b–c)). The position of solid contact in the DEM occurs at a distance d between the particles centres, allowing an overlap of the α function of the two particles of $2l_c$. To finish with, we assume the solid contact to be rigid enough, then the length scale of deformation of the solid remains small compared with these lengths. The solid contact is resolved using the DEM and is parametrized by the restitution e and the solid friction μ_p.

In the following sections, we will investigate the influence of (σ, l_c) on the dynamics of the immersed collapse. According to the numerical roughness length discussed previously, the function α satisfies $\alpha(|\boldsymbol{x} - \boldsymbol{x}_j| = d/2 + l_c - \sigma) = 0.5$ where $\boldsymbol{x}_j$ is the position of a particle centre j. For $l_c > 0$, particles close to solid contact imply an overlap of the function α prescribed to each individual particle. In the state of our knowledge, the link between this overlap and the one of real grains remains difficult to quantify. We propose here to consider first $l_c = \sigma$ which will also be referred to as case $R = R_o$ in the following (figure 2(b)). Then, we consider the opposite situation for which solid contact would occur at the summit of roughness, i.e. $l_c = 0$, referred to as case $R = R_i$ (figure 2(c)). σ then refer to the amplitudes of the numerical roughness. Note, that when σ goes to zero, the two situations become identical and mimic a smooth sphere. However, and as already mentioned, this smooth situation is unreachable in our configuration as it also necessitates $\Delta x_I \ll d$.

In the next section, figures thus come with small vignette sketching the associated IBM weight function (as sketched in figure 2). For R_0 the fluid-solid interface spreads slightly out of the sphere of diameter d on a length scale $\sigma/2$. This is materialized in the associated vignettes by a dash line at which the IBM weight function α goes to zero while the solid line corresponds to the DEM particle radius at which solid contact occurs. On the other hand, R_i corresponds to a configuration for which the fluid-solid interface is entirely in the solid sphere, i.e. $\alpha = 0$ at the surface of solid contact between particle. In small vignettes, dash lines and solid lines thus coincide.

1.3. *Details of the simulations*

The set-up is similar to the one describe in the main paper. Nevertheless, for the IBM/DEM approach, the cost of a simulation is known to be the main limitation, requiring to decrease the number of grains which can be reasonably simulated. Microscale simulations (IBM/DEM) and mesoscale simulations (VANS/DEM) presented and confrontedd in the following are thus performed for a reduced number of grains within the collapse compared to the one used along the main paper. For now on, we choose $d = L_i/16$, keeping $a = 0.5$. The size of the total domain remains $L_x \approx 3L_i$ and $L_y \approx 0.8L_i$ in the vertical plane. In the third direction, we set $L_z = 5d$ for the IBM/DEM simulations and $L_z = 40d$ for the VANS/DEM simulations. For the latter, keeping a

Method	a	L_i/d	L_z/d	ϕ_i	r	St	$d/\Delta x_I$	σ/d	R (l_c/σ)
IBM/DEM	0.5	16	5	0.58	1.6	0.5	20	$[0.0325, 0.065]$	$[R_o, R_i]$ $([1, 0])$
VANS/DEM	0.5	16	40	0.58	1.6	0.5	–	–	–

TABLE 1. Range of dimensionless parameters covered in the paper, and more particularly in each section.

reasonable length of resolution of the fluid phase to resolve fluid velocity gradient in the main flow plane (x, y) imposes to reduce the mesh size $(\Delta x_V, \Delta y_V)$ compared to the grain size d, such as $\Delta x_V = \Delta y_V = d$. With the present method, stability of the numerical method is mostly associated with the minimum number of grains required in a fluid cell for the averaging procedure from the Lagrangian description, DEM, to the Euler description, VANS. It thus imposes to widen VANS cells in the spanwise direction such as $\Delta z_V \approx 10d$. Given the relative importance of the (x, y) description and invariance of the averaged fluid flow in the z one, for the present collapse configuration, it has been shown that this choice allows to refine the description of the granular flow and its associated final rest state.

Again, to keep a reasonable computational cost, the fluid and particles properties η, ρ and ρ_p are fixed in this section, leading to constant value of St and r according to their definition given in the main paper. In particular, we choose here $St = 0.5$ and $r = 1.6$, corresponding typically to glass beads of 150 μm diameter immersed in water.

For the IBM method proposed here among others, it is now well established that spatial resolution $d/\Delta x_I$ has a crucial influence on the numerical resolution. Regarding previously obtained results (Izard *et al.* 2014; Pierson & Magnaudet 2018), and to limit the computational cost of one simulation, we perform simulations using $d/\Delta x_I = 20$. As mentioned previously, it has to be complemented with configuration R and σ/d at the interfacial scale, which are crucial to model the dynamics close to contact. We have performed four simulations $R = [R_o, R_i]$ (or equivalently $l_c = [\sigma, 0]$) and $\sigma/d = [\sigma_1/d, \sigma_2/d] = [0.065, 0.0325]$. Note that in any case, $2\sigma > \mathcal{O}(\Delta x_I)$, i.e. the transition length from the inner part of a particle to its outer part is larger that the numerical cell.

The set of parameters used in the following for both the IBM/DEM simulations and VANS/DEM simulations is summarized in table 1.

2. Immersed collapse from the IBM/DEM simulations

The objective of the section is to highlight the influence of the numerical parameter $(R, \sigma/d)$ on the collapse. This will be discussed in term of the interstitial fluid dissipation.

2.1. *Dynamics of the collapse at the micro-scale*

A first qualitative highlight of the collapse using the IBM-DEM method can be seen in figure 3 for all $(R, \sigma/d)$ considered here. In particular, the 2D-temporal-trajectories of the mass centre of each grain in (x, y) are shown. As usually observed for a granular collapse at small aspect ratio, $a = 0.5$ here, most of the granular flow is localised close to the front of the granular medium and the final deposit has a trapezoidal shape. Note that the granular medium remains relatively dense during the whole collapse, and static close to the back wall $x = 0$. These observations are actually quite similar for the different couples $(R,\ \sigma/d)$. However, some differences can be highlighted particularly on the dynamics.

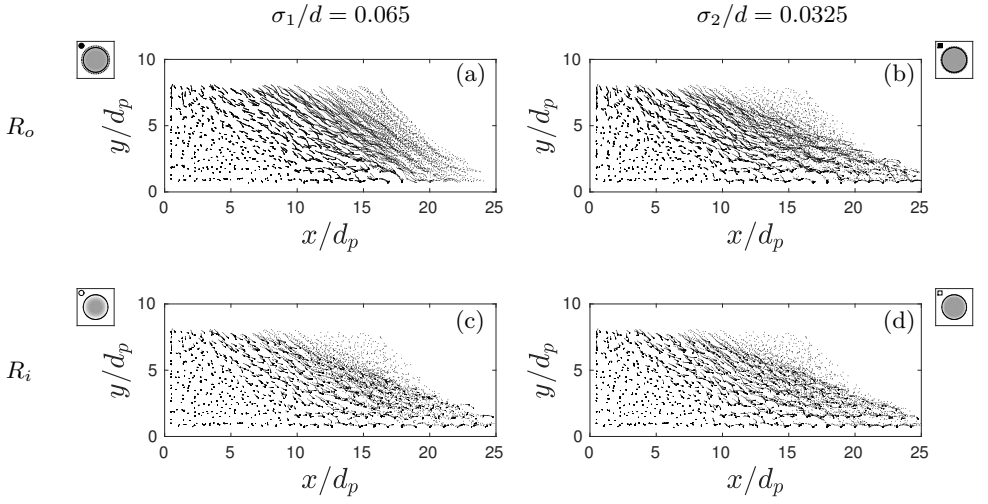

FIGURE 3. Particle trajectories during the collapse (IBM/DEM), highlighting static regions and inertial regions, for the different couples $(R, \sigma/d)$. Here, the position of the centre of mass of each grain is symbolized by a dot and superimposed at different time with a constant time step Δt. Time lag between snapshot is $\Delta t\sqrt{g/H_i} \approx 1$. Note that grains remains in close contact during the whole collapse.

Apparent continuous trajectories for $(R,\ \sigma/d) = (R_o,\ 0.065)$ indicate a slower dynamics than the other cases. A higher dissipation during the collapse is therefore anticipated for this situation. A closer inspection indicates that particles evolve more quickly over their trajectories for R_i (isolated dots on the upper right corner of the granular medium in figure 3) than for R_o. This indicates that fluid dissipation is probably more efficient for R_o than R_i.

In order to quantify more clearly the above mentioned observations, the motion of the granular material is characterized by the position of its centre of mass (X_g, Y_g) and spreading length (front position) X_f during the collapse. In particular, the temporal evolutions of $(2X_g - L_i)/L_i$ and $(2Y_g - H_i)/H_i$ (these definition are used for convenience as the initial position of the centre of mass is $(0, 0)$ in its dimensionless form) are plotted in figure 4(a) and figure 4(b) respectively, while the temporal evolution of $(X_f - L_i)/L_i$ is shown in figure 4(c). $(H_i/g)^{1/2}$ has been chosen here as the characteristic time scale. The different symbols in all these figures correspond to the different values of $(R, \sigma/d)$ as sketched in figure 2 and reported at the bottom of figure 4. Even if the curves in figure 4 have a similar temporal evolution for the different $(R, \sigma/d)$, a quantitative difference is obtained. This difference concerns mostly the characteristic time of evolution rather than the final rest state, as observed in figure 3 and also reported in figure 7(a).

Figure 4 thus indicates that the values of $(R,\ \sigma/d)$ influence the dynamics of the collapse while the final state is not significantly affected. In particular, the time scale of the granular slumping for the different cases shows that dissipation decreases from $(R,\ \sigma/d) = (R_o, 0.065)$ to $(R,\ \sigma/d) = (R_i, 0.065)$ with $(R,\ \sigma/d) = (R_o, 0.0325)$ and $(R,\ \sigma/d) = (R_i, 0.0325)$ being intermediate situations. More generally, configurations R_i (open symbols), i.e. $l_c = 0$, are less dissipative than cases R_o (full symbols), $l_c = \sigma$. Moreover, the smaller σ/d is the more comparable are situations R_i and R_o (square

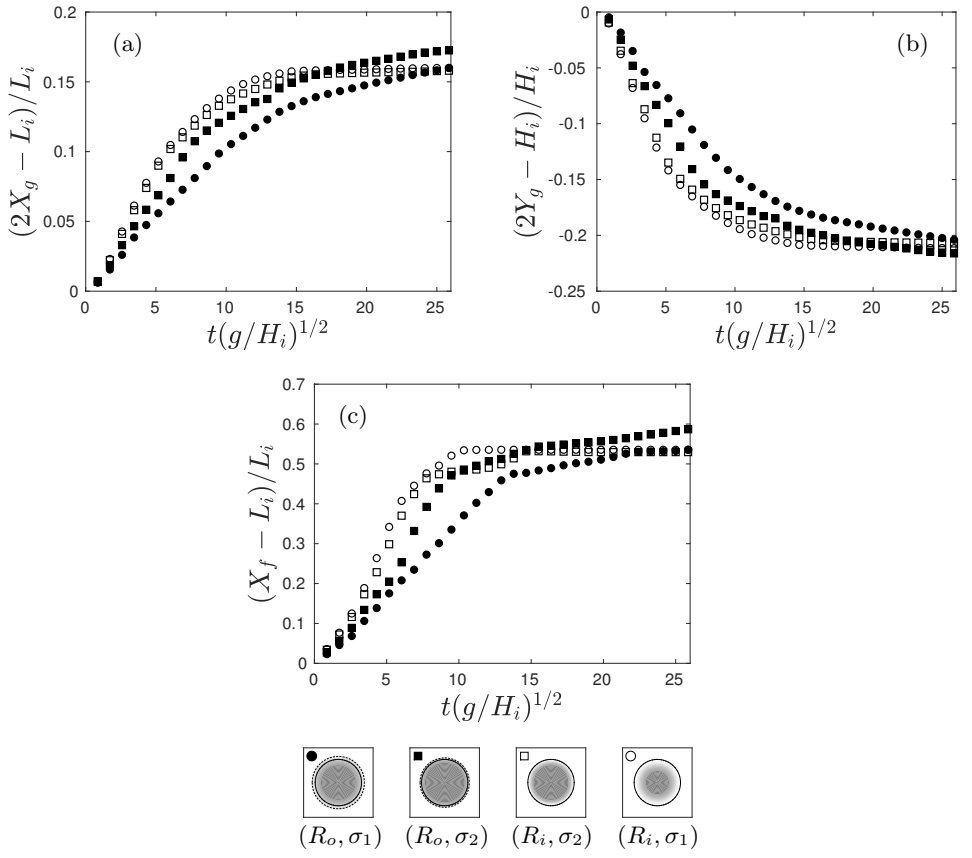

FIGURE 4. Temporal evolution of the characteristic lengths of the granular medium (IBM/DEM): centre of mass position (X_g, Y_g) (a-b) and front position X_f (d) as function of time, in their dimensionless form as explained in the text. Symbols are recalled in vignettes (bottom row) sketching the four couples (R, σ).

symbols), consistent with the fact that the two situations should converge when σ/d goes to zero, as already mentioned.

2.2. *Fluid dissipation in the porous granular medium*

In order to understand qualitatively the different spreading time scales of the collapse, we discuss the previous results in terms of volume fraction of the interstitial fluid. For all $(R, \sigma/d)$, properties of the fluid and the grains are the same, the only difference being on the interface shape between the solid phase and the fluid phase. Then one defines the interstitial fluid fraction of the initial state $\varepsilon_{pore|i}$, where subscript i stands for initial, within the granular material, as

$$\varepsilon_{pore|i} = 1 - \phi_{solid|i} \quad \text{with} \quad \phi_{solid|i} = \frac{N_p \mathcal{V}_{solid|j}}{H_i L_i L_z}, \tag{2.1}$$

with $\mathcal{V}_{solid|j} = \int \alpha_j dV$ for particle j. This differs from the more standard definition ϕ_i which characterizes a geometrical volume fraction based on the diameter of the particle d, as the length scale between particle centres in contact. Note that the volume fraction

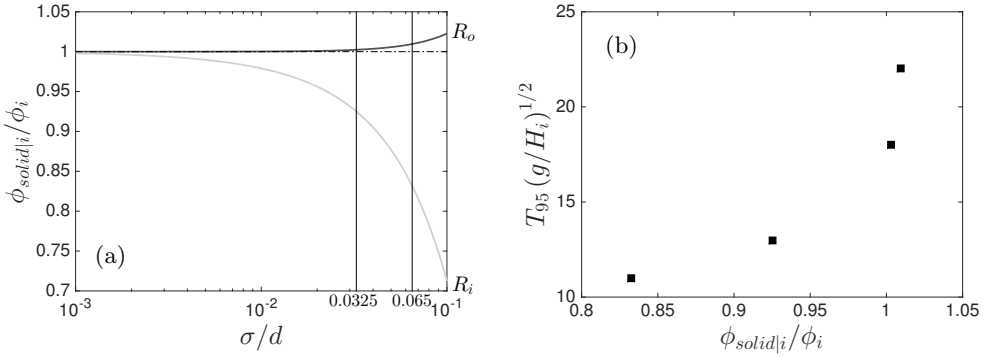

FIGURE 5. (a) Evolution of $\phi_{solid|i}/\phi_i$ as a function of the apparent roughness length σ/d for R_o (dark grey line) and R_i (light grey line). The two vertical thin lines correspond to the values of σ/d considered in this study. (b) Dimensionless spreading time $T_{95}\sqrt{g/H_i}$ as a function of $\phi_{solid|i}/\phi_i$.

measured in experiments is more likely to be ϕ_i. Obviously both definitions coincide for perfectly smooth grains, i.e. $\sigma = 0$. Here, unlike ϕ_i, which is constant in this supplementary material, $\varepsilon_{pore|i}$, or equivalently $\phi_{solid|i}$, varies with (R, σ).

The ratio $\phi_{solid|i}/\phi_i$ is shown as a function of σ/d for the two cases R_o and R_i in figure 5(a). In particular, the dark grey line correspond to R_o while the light grey line corresponds to R_i. It is thus shown here that $\phi_{solid|i}/\phi_i$ strongly depends on both R and σ/d. The most drastic influence is R which can lead to $\phi_{solid|i} > \phi_i$ (R_o) or $\phi_{solid|i} < \phi_i$ (R_i). The former case is easily understandable, the solid can not spread out of the sphere d, then necessarily $\phi_{solid|i} < \phi_i$. Moreover, the thicker is the interface the smaller is $\phi_{solid|i}$. This explains the trend of the light grey curve in figure 5(a). On the other hand, the case R_o is slightly less obvious. In this case, as the solid phase spreads out of sphere d (see figure 2(a-b)) it is possible to have $\phi_{solid|i} > \phi_i$. This actually depends on the shape of the α function at the interface, and appears to be the case for R_o. Now as $\phi_{solid|i} > \phi_i$, the ratio $\phi_{solid|i}/\phi_i$ necessarily decreases with decreasing σ as it has to reach 1 for $\sigma = 0$. Based on this observation, it is possible to order the four cases considered here from small to high value of $\phi_{solid|i}/\phi_i$ as $(R_i, \sigma_1/d)$, $(R_i, \sigma_2/d)$, $(R_o, \sigma_2/d)$ and $(R_o, \sigma_1/d)$. Accordingly, as a quantifier of the influence of the dissipation, the dimensionless time scale of the granular collapse $T_{95}(g/H_i)^{1/2}$ is plotted as a function of $\phi_{solid|i}/\phi_i$ for the four cases in figure 5(b). (T_{95} is defined as in the main body of the paper.) One observes here that the collapse time scale increases with increasing $\phi_{solid|i}$, or equivalently decreasing $\varepsilon_{pore|i}$, i.e. for decreasing available volume for fluid to flow.

It has therefore been shown that the different cases considered here lead to different viscous dissipations induced by the interstitial fluid. This effect can be linked to the effective properties of the fluid-solid interface. In particular, increasing $\phi_{solid|i}/\phi_i$ leads to a decrease of the available fluid allowed to flow in the gap between two particles in solid contact (a distance scale of $d + l_c - 2\sigma$ as shown in figure 2(a)). Unfortunately, an objective quantification and the link with roughness scales of reals grain are hardly reachable as it would require controlled-multi-scale laboratory experiments, which are difficult to perform, as well as more resolved microscale simulations in order to decrease

more significantly σ/d. The latter point remains numerically expensive, and probably unfeasible in the state. This is for now well beyond the scope of the present paper and would deserve dedicated configurations.

3. Validation of mesoscale closures through microscale simulations.

The objective of the section is to discuss the relevance of the closure models –rels. (2.6) and (2.8) in the main paper– used for the VANS/DEM simulations along the main paper. Recall that these models are

$$n\mathbf{F}_D^M = \frac{18\eta}{d^2}\phi\left(1-\phi\right)^{-\xi}\left(1+\frac{1}{60}\mathrm{Re}_p\right)\left(\langle\mathbf{v}\rangle_p - \langle\mathbf{u}\rangle_f\right), \tag{3.1}$$

$$\eta_{eff}^M/\eta = 1+\frac{5}{2}\phi+7.6\phi^2+\zeta\phi^3, \tag{3.2}$$

for the effective drag and effective viscosity respectively.

3.1. *Upscaling: from the microscale model to the mesoscale model*

The consequence of the influence of (R,σ) is first discussed in term of drag model and effective viscosity model used as closure terms for the mesoscale approach. For this purpose, we first describe the upscaling approach to extract these terms from the microscale simulations.

In order to be consistent with equations (1.1) and (1.2), i.e. with the resolved approach (IBM), the fluid-particle interaction force $\langle\mathbf{f}_{p/f}\rangle_p$ and the effective fluid stress $\mathbf{S}$ appearing at the mesosale and modeled for the VANS method (see main paper), should be expressed as (similarly to Yu & Shao 2007; Gallier *et al.* 2014),

$$n\langle\mathbf{f}_{p/f}\rangle_p = \frac{1}{\mathcal{V}}\sum_{j\in\mathcal{V}}\left(\rho\frac{D}{Dt}\int\limits_{\mathcal{V}_j}\mathbf{u}dV - \int\limits_{\mathcal{V}_j}\mathbf{f}_j^{ibm}dV - m_j^f\mathbf{g}\right), \tag{3.3}$$

$$\text{and}\quad \mathbf{S} = \langle\mathbf{S}\rangle_f + \langle\mathbf{S}\rangle_p, \tag{3.4}$$

with

$$\langle\mathbf{S}\rangle_f = \frac{1}{\mathcal{V}}\int\limits_{\mathcal{V}}(1-\alpha)\left[\sigma_f - \rho(\mathbf{u}-\langle\mathbf{u}\rangle_f)\otimes(\mathbf{u}-\langle\mathbf{u}\rangle_f)\right]dV, \tag{3.5a}$$

$$\langle\mathbf{S}\rangle_p = \frac{\rho}{\mathcal{V}}\sum_{p\in\mathcal{V}}\int\limits_{\mathcal{V}}\left[(\mathbf{x}-\mathbf{x}_p)\otimes\left(\alpha\frac{D\mathbf{u}_f}{Dt}-\mathbf{f}_j^{ibm}\right)\right]dV. \tag{3.5b}$$

In the previous expression, the fluid stress tensor has been defined as $\sigma_f = -p\mathbf{I} + [\eta\left(\nabla\mathbf{u} + {}^t\nabla\mathbf{u}\right)]$. Note that the averaging procedure used to calculate the integral quantities in (3.3) and (3.5) from the IBM/DEM simulations, includes a gaussian weight function in the (x,y) plane, decreasing from the centre of the cell $\mathcal{V}$ to smooth out edge effect, and invariant in the z direction. The standard deviation of this gaussian weight function is d. A cut-off length of this weight function is set at $3d$ beyond which its influence on the integral terms becomes negligible. This weight function has not been explicitly written in (3.3) and (3.5) for sake of clarity.

According to the assumptions made for the fluid-particle force in the paper, only a drag

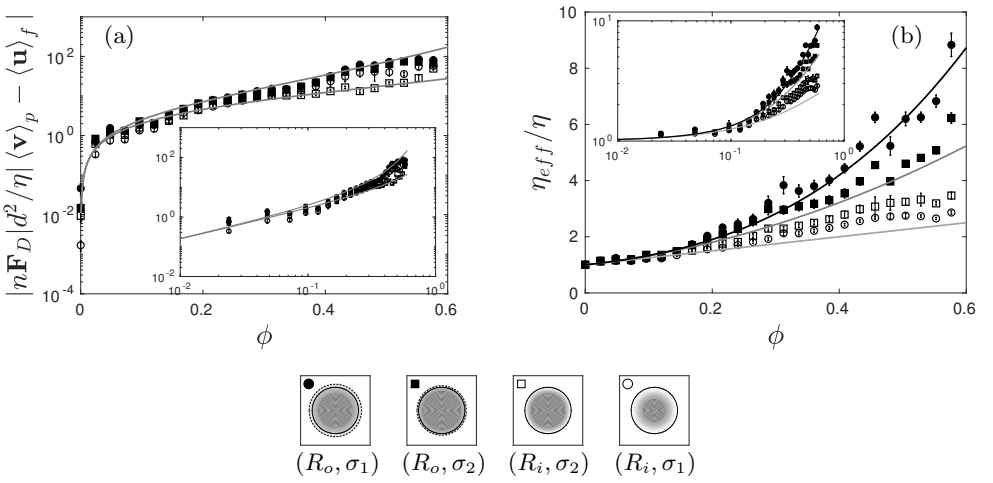

FIGURE 6. Dimensionless effective drag force $|n\mathbf{F}_D|d^2/\eta|\langle\mathbf{v}\rangle_p - \langle\mathbf{u}\rangle_f|$ as a function of ϕ (a) and dimensionless effective viscosity η_{eff}/η as a function of ϕ (b). Symbols are recalled in vignettes (bottom row) sketching the four couples (R, σ). Solid lines in (a) correspond to model (3.1) with $\xi = 1$ (lower curve) and $\xi = 3$ (upper curve), while solid lines in (b) correspond to (3.2) from the $\mathcal{O}(\phi)$ (light grey) to the $\mathcal{O}(\phi^3)$ (black) approximation (see text for details).

contribution is extracted here. We assume that the drag contribution can be extracted from the IMB simulations as

$$|n\mathbf{F}_D| = \frac{\varepsilon n}{|\langle\mathbf{v}\rangle_p - \langle\mathbf{u}\rangle_f|} \left\langle -\frac{1}{\mathcal{V}} \sum_{j\in\mathcal{V}} \int_{\mathcal{V}_j} \mathbf{f}_j^{ibm} dV \right\rangle_p \cdot (\langle\mathbf{v}\rangle_p - \langle\mathbf{u}\rangle_f)\,. \tag{3.6}$$

Note that given the dimensionless parameters $St = 0.5$ and $r = 1.6$ used here, the inertial contribution of the drag force can be disregarded as Re_p remains smaller than one. Then, the drag force is a linear function of the slip velocity $|\langle\mathbf{v}\rangle_p - \langle\mathbf{u}\rangle_f|$. In this case $|n\mathbf{F}_D|d^2/\eta|\langle\mathbf{v}\rangle_p - \langle\mathbf{u}\rangle_f|$ is thus sought as a function of only ϕ. The results obtained accordingly from the microscale simulations are summarized in figure 6(a). Note that ϕ depends on space and time during the collapse, leading to values covering a wide range of volume fraction in a single collapse. Then each set of symbols in figure 6 corresponds to a single collapse. For sake of clarity, the results shown here correspond to mean values over several raw data as explained in Annexe A. The obtained results are compared with model (3.1) ($Re_p = 0$), with $\xi = 1$ (lower solid curve) and $\xi = 3$ (upper solid curve).

Similarly, the effective viscosity of the fluid phase at a scale larger than each individual grain can be obtained by averaging results obtained with IBM/DEM simulations. In particular, one can define an effective viscosity such as

$$\eta_{eff} = \|\boldsymbol{\tau}\|/\|(\nabla\langle\mathbf{u}\rangle + {}^t\nabla\langle\mathbf{u}\rangle)\|, \tag{3.7}$$

with $\boldsymbol{\tau}$ the deviatoric part of the stress tensor $\mathbf{S}$ in (3.4), and $\|\cdot\|$ denoting the second invariant of a tensor. As for the drag model, in the viscous regime considered here η_{eff}/η should also be a function of only ϕ as modelled in (3.2). Results are shown in figure 6(b). Again, each set of symbols corresponds to averaged values, as explained in Appendix A, of a single collapse corresponding to a set of parameters $(R, \sigma/d)$. Results are compared with model (3.2), such as only the Einstein viscosity at $\mathcal{O}(\phi)$ is considered (light grey

line), then extended to the Batchelor viscosity at $\mathcal{O}(\phi^2)$ (dark grey line), and then the full model (3.2) with $\zeta = 16$ (obtained here as a numerical fitting parameter).

One can conclude that, for both the drag and effective viscosity (figure 6(a)-(b)), the different models chosen for the VANS/DEM approach and discussed in the paper are consistent with the results obtained with the IBM/DEM simulations, i.e. extracted from microscale simulations. It is shown that the obtained values for the parameter $\xi \in [1, 3]$ in (3.1) and the order of pertinence of the viscous model (3.2) depend on the fluid-solid interface modelling in the microscale approach. In particular, R_o induces a stronger viscous resistance than R_i, in which the value of σ/d also plays a role. Note that the sorting of the $(R, \sigma/d)$ parameters in term of the importance of fluid dissipation is in lines with the one obtained from the spreading of the granular material, discussed in figure 4. This also confirms the influence of $(R, \sigma/d)$ attributed to the available fluid fraction with the granular column, discussed in figure 5, as increasing $\phi_{solid|i}/\phi_i$ induces an increase of the fluid dissipation.

3.2. *Comparison of the microscale model and the mesoscale model*

3.2.1. *Influence of the drag force model*

According to the results obtained in the previous section, we model the drag force at the mesoscale (VANS) as,

$$n\mathbf{F}_D^M = \frac{18\eta}{d^2}\phi\,(1-\phi)^{-\xi}\,(\langle\mathbf{v}\rangle_p - \langle\mathbf{u}\rangle_f)\,, \tag{3.8}$$

with three different values of ξ such as $\xi = [1, 2, 3]$. For the effective viscosity, the following model is used, i.e. the first order contribution of (3.2)

$$\eta_{eff}^M/\eta = 1 + \frac{5}{2}\phi. \tag{3.9}$$

Comparisons are shown in figure 7. In particular, IBM/DEM results correspond to $(R, \sigma/d) = (R_i, 0.065)$, $(R, \sigma/d) = (R_o, 0.0325)$ and $(R, \sigma/d) = (R_o, 0.065)$ with their associated symbols given in the figure. Moreover, solid lines correspond to the VANS/DEM model, with $\xi = 1$ (light grey lines), $\xi = 2$ (dark grey lines) and $\xi = 3$ (black lines). First, the shape of the final deposit is compared in figure 7(a). This first comparison is provided to show that whatever the model (IBM vs. VANS) but also the parametrization of the roughness in the IBM and the value of ξ for the effective drag, the system evolves towards roughly the same final deposit. This is a first highlight on the pertinence of the model used for the mesoscale approach (VANS/DEM), keeping the interaction closure terms as simple as possible.

The dynamics of the morphology of the deposit is compared in figures 7(b). In particular, the dimensionless front position $(X_f - L_i)/L_i$ (b.1), the dimensionless horizontal and vertical positions of the centre of mass $(2X_g - L_i)/L_i$ (b.2) and $(2Y_g - H_i)/H_i$ (b.3), respectively, are plotted as a function of $t(g/H_i)^{1/2}$. We observed that the dynamics is very well captured by the proposed mesoscale model with an accuracy of the grain diameter d (see vertical lines in figures 7(b) which shows the grain length in these scales).

A further confrontation concerns averaged energy over the granular material. In figures 7(c), the evolutions of the dimensionless potential energy E_p/E_p^0 (c.1), the dimensionless kinetic energy E_k/E_p^0 (c.2) and the dimensionless rotational kinetic energy E_k^{rot}/E_p^0 (c.3), of the granular phase, are compared. First, note that the energy is dominated by the potential energy. Both the potential energy and the kinetic energy are relatively well captured by the mesoscale model. Even if the microscale approach shows an evolution of the kinetic energy which is slightly more complicated, the order of magnitude of its

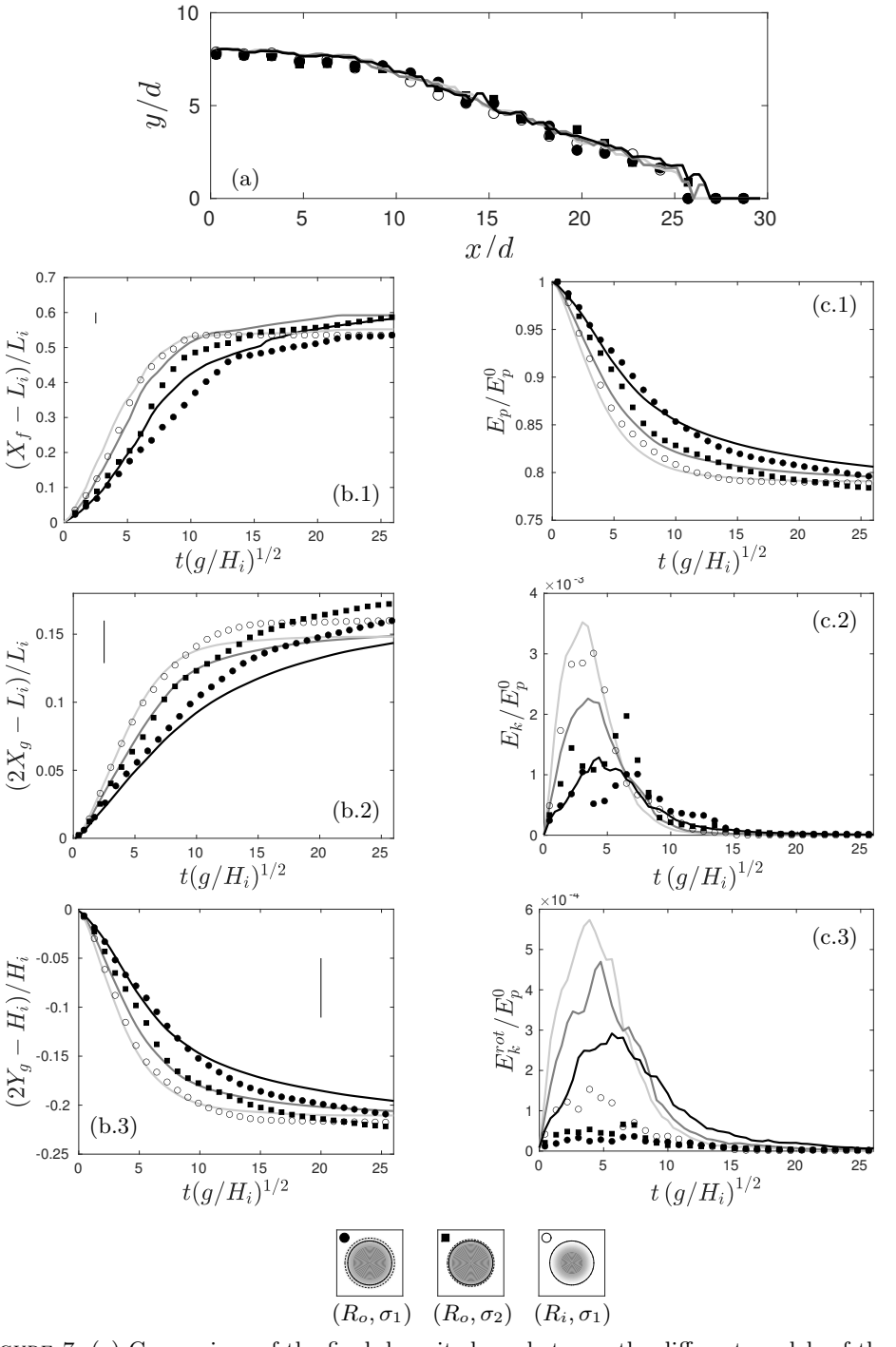

FIGURE 7. (a) Comparison of the final deposit shape between the different models of the IBM and VANS simulations. (b–c) Comparisons of the temporal evolution of the characteristic lengths (b) and characteristic energies averaged over the granular material (c): IBM/DEM (symbols) and VANS/DEM (lines). Details of the parameters used in each model and leading to results represented by the light grey, dark grey and black lines are given in the text. Thin vertical lines in (b) show the typical length scale corresponding to a grain diameter.

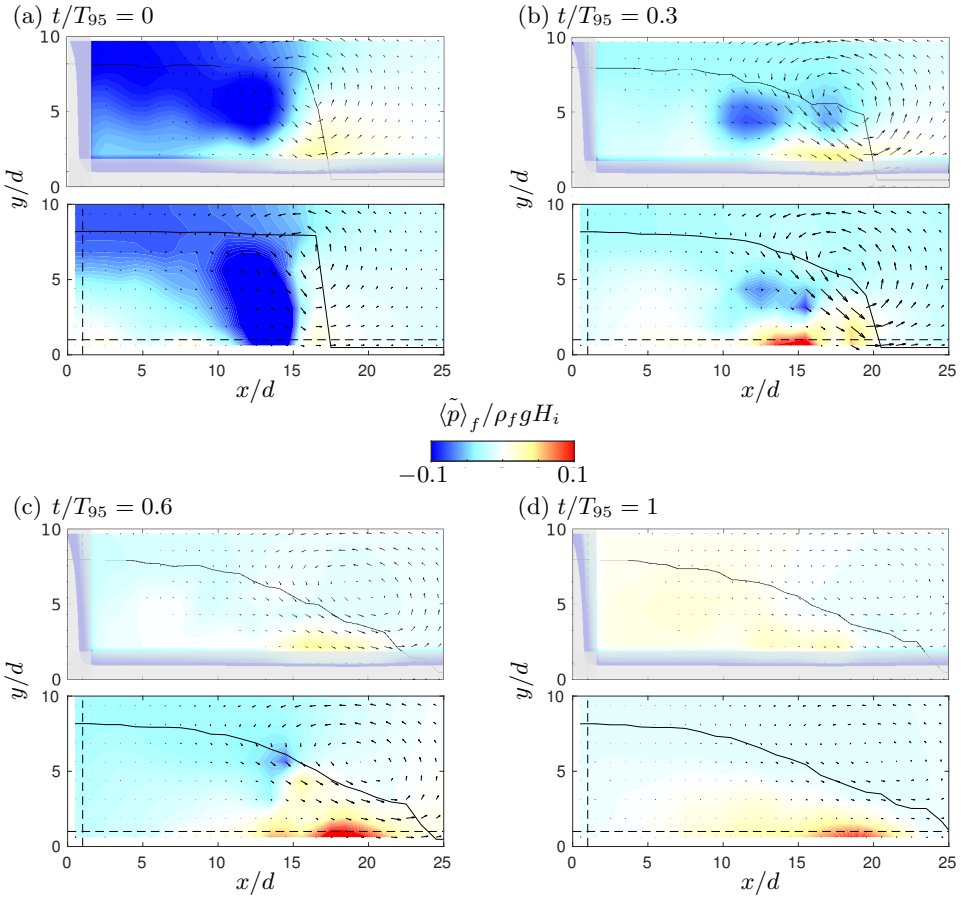

FIGURE 8. Comparisons of the temporal evolution of dimensionless pressure field $\langle\tilde{p}\rangle_f/\rho_f g H_i = \left(\langle p\rangle_f - \rho g(L_y - y)\right)/(\rho_f g H_i)$ (contour color) and velocity fields (vectors): IBM/DEM (upper rows in (a–d)) and VANS/DEM (lower rows in (a–d)). The height profiles $h(x,t)$ extracted from the upper position of particles on the granular pile are plotted as solid lines. Details of the parameters used in each model are given in the text. Solid lines show the shape of the granular medium at the corresponding time. In IBM/DEM figures (upper rows), light grey zone correspond to the region in which mean pressure estimation is influenced by the boundaries, and that should therefore be disregarded. In VANS/DEM figures (lower row), dashed lines delineate the first VANS mesh cell at the boundary from the bulk.

amplitude between the two approaches is in reasonable agreement. Nevertheless, the rotational contribution is not well captured. As shown in figure 7(c.3), its amplitude is small, meaning that rotation is not a key parameter on the dynamics of the collapse for the range of parameters considered here, but it can be anticipated that extension towards configurations with more rotation could generate disagreement between microscale and mesoscale methods. This has to be attributed to the simple interaction force model used here for the mesoscale approach which does not provide any fluid torque contribution to the particle motion. Then torque is only provided through solid contact at the mesoscale. The microscale shows that this contact-induced rotation is counterbalanced by a viscous part induced by the fluid.

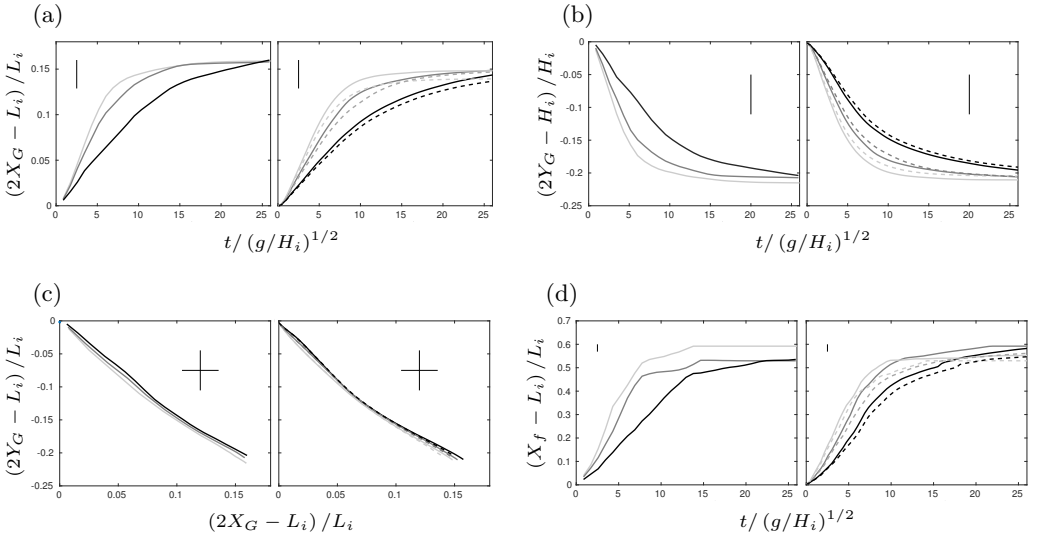

FIGURE 9. Comparisons of the temporal evolution of the characteristic lengths as in figure 4: IBM/DEM (left columns in (a–d)) and VANS/DEM (right columns in (a–d)). Details of the parameters used in each model and leading to results represented by the light grey, dark grey and black lines are given in the text. Thin vertical line (a,b,d) and thin cross (c) show the typical length scale corresponding to a grain diameter.

To finish with, comparisons on the fluid phase are discussed. For this purpose, snapshots of the fluid relative pressure, $\langle\tilde{p}\rangle_f = \langle p\rangle_f - \rho g(L_y - y)$, are shown in figure 8. Moreover, the velocity field is shown with the velocity vectors, as black arrows. Here, the case $(R, \sigma/d) = (R_o, 0.065)$ of the IBM/DEM model (top panels in figure 8) is compared with the case $(\xi = 1, \eta_{M|f}/\eta = 1 + \frac{5}{2}\phi)$ of the VANS/DEM model (bottom panels in figure 8). Note that the same scales for pressure and velocity field are used here for the two methods. The same patterns of spatio-temporal pressure are observed with the two approaches. It can be noted that a negative pressure is generated at very early stages, meaning that the column needs to dilate priori collapsing. Then, a positive pressure pattern quickly appears at the bottom of the column. Even if the order of magnitude of these pressure patterns are slightly different, we can see that the mesoscale approach capture most of the fluid dynamics. Moreover, the collapse generates a vortex at the upper corner of the initial column, which then follows the front. Note that this fluid structure could play a role on the transport, at least close to the upper surface of the granular materials. However, this influence is expected (in the state of our knowledge) to be second order contribution compared to the gravity induced motion, and is therefore postponed to a future dedicated work. To finish with, the observed pressure patterns suggest a first dilatancy of the granular medium and then a compaction close to the bottom. This is not clear whether one dominates the other on the dynamics. This suggest that the initial volume fraction $\phi_i = 0.58$ is probably quite close to the transition between the "loose-packing" and "dense-packing" as discussed in the main paper.

3.2.2. *Influence of the effective fluid viscosity model*

An extra comparison between the IBM/DEM results and the VANS/DEM is shown in figure 9. We focus here on the influence of the effective viscosity model on the evolution of the morphology of the collapse (similar to figure 7). In particular, left panel corresponds to the IBM/DEM simulations for $(R, \sigma/d) = (R_i, 0.065)$ (light grey lines), $(R, \sigma/d) =$

$(R_o, 0.0325)$ (dark grey lines) and $(R, \sigma/d) = (R_o, 0.065)$ (black lines), while right panel correspond to the VANS/DEM model, with $\xi = 1$ (light grey lines), $\xi = 2$ (dark grey lines) and $\xi = 3$ (black lines), dashed lines being for the full viscosity model (3.2) and solid lines its order ϕ version (Einstein viscosity), i.e. model (3.9). In all figures, horizontal and vertical solid lines correspond to the grain diameter d length scale. One shows here that the influence of the effective viscosity model remains smaller than the influence of the drag model.

4. Conclusion

Considering the smallest scale which can be resolved for multi-contact granular configurations with one of the state of the art of numerical methods available –the IBM/DEM approach–, results have shown to be sensitive to the local description of the flow in between solid particles, revealed here by the transition of the IBM weight α. The local description chosen here is an alternative approach to deal with the complex issue of solid contact in a viscous fluid, which is singular for perfectly smooth and rigid grains. For that purpose the interface between the grain and the fluid is diffused through this numerical solid fraction α, and then shares similitude with a porous shell. This is done in the light of our knowledge on the possible influence of roughness in the case of real grains. This fluid-particle interface is parametrized by two numerical parameters l_c and σ, or equivalently R and σ. R characterizes the localisation of the interface with respect to the position of the particle surface considered for the solid contact, to be associated with a length scale l_c (figure 2(a)). The two cases considered here are referred to as R_o and R_i. R_o corresponds to a configuration for which $l_c = \sigma$. On the other hand, for the R_i configuration, $l_c = 0$. σ then corresponds to the length scale of the interface. The influences of these parameters on the dynamics of the collapse have been attributed to the available pore fraction for the fluid phase, leading to a dimensionless parameter $\phi_{solid|i}/\phi_i$ which can be different from one to the other couple $(R, \sigma/d)$. The viscous dissipation associated with the fluid phase is thus dependent on this parameter.

The effective viscosity of the fluid phase at a scale larger than one grain, as well as the effective drag force, both characterizing fluid-particle dissipation, have been extracted from the IBM/DEM results, also showing an influence of $(R, \sigma/d)$. Effective viscosity and effective drag are shown to be consistant with models from the literature. The role of $(R, \sigma/d)$ on the parameters of these models are consistent with their role on the dynamics through the influence of $\phi_{solid|i}/\phi_i$. Theses models have thus been used in the mesoscale approach as closure terms.

Using these effective models, mesoscale simulations (VANS/DEM) have been compared to the microscale simulations (IBM/DEM). The mesoscale approach has been shown to be relevant to capture the main processes of the immersed granular collapse. In particular, the influence of the numerical roughness at the microscale is simply captured by modifying the effective models at the mesoscale in the range of models found in the literature. For now, these results remain preliminary and would require a deeper investigation, but this seems promising for future works dealing with the influence of surface roughness on the dynamics of granular flows. Moreover, some discrepancies between the approaches have been highlighted. They can be attributed to the assumption of modelling fluid-particle force through a single drag force. Improvement could also be provided on this point in future works.

According to the objectives of the main paper, the influence of $(R, \sigma/d)$ and the related choice of closure models were found to remain relatively small compared to the influence of (St, ϕ_i) summarized in the main body of the paper.

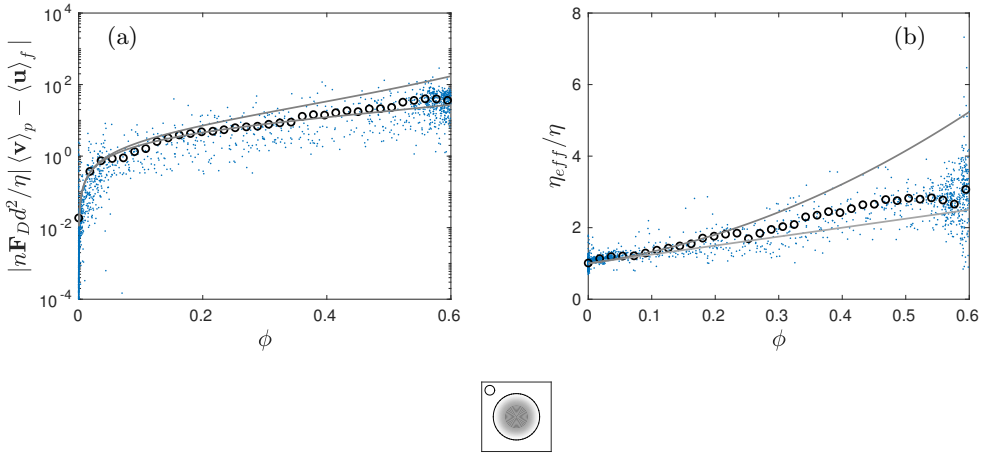

FIGURE 10. Dimensionless effective drag force $|n\mathbf{F}_D|d^2/\eta|\langle\mathbf{v}\rangle_p - \langle\mathbf{u}\rangle_f|$ as a function of ϕ (a) and dimensionless effective viscosity η_{eff}/η as a function of ϕ (b), for couple $(R, \sigma/d) = (R_i, 0.065)$. Blue dots correspond to the full data set while black symbols are the average values as used in figure 6. Lines correspond to model (3.1) and (3.2) for the drag and the effective viscosity (order ϕ and order ϕ^2 shown here), respectively.

Appendix A. Averaging closure terms from IBM/DEM simulations

The results obtained for the effective drag force and the effective viscosity from the IBM/DEM simulations and shown in figure 6 have been obtained through an average of the rough data extracted using (3.6) and (3.7). This representation has been chosen for sake of clarity on this plots. Rough data are much more dispersed regarding the small domain that can be simulated with the IBM/DEM model. Here, an example of the obtained rough data and their average extraction is shown in figure 10 for both the drag and viscosity. Note that the average is obtained by considering that the effective dimensionless drag $|n\mathbf{F}_D|d^2/\eta|\langle\mathbf{v}\rangle_p - \langle\mathbf{u}\rangle_f|$ and the dimensionless effective viscosity η_{eff}/η are function of the single variable ϕ (see dot in figure 6). Mean values of drag and viscosity are then obtained by a sliding window average, weighted by a gaussian function, over ϕ (see black symbols in figure 6). Even if results are quite dispersed, such approximation can be considered as valid as a first order approximation, leading to acceptable trends following well established models.

REFERENCES

ARDEKANI, A. M .AND RANGEL, R. H. 2008 Numerical investigation of particle–particle and particle–wall collisions in a viscous fluid. *J. Fluid Mech.* **596**, 437–466.

BIGOT, B., BONOMETTI, T., LACAZE, L. & THUAL, O. 2014 A simple immersed-boundary method for solid–fluid interaction in constant-and stratified-density flows. *Computers Fluids* **97**, 126–142.

GALLIER, S., LEMAIRE, E., PETERS, F. & LOBRY, L. 2014 Rheology of sheared suspensions of rough frictional particles. *J. Fluid Mech.* **757**, 514–549.

IZARD, E., BONOMETTI, T. & LACAZE, L. 2014 Modelling the dynamics of a sphere approaching and bouncing on a wall in a viscous fluid. *J. Fluid Mech.* **747**, 422–446.

IZARD, E., LACAZE, L., BONOMETTI, T. & PEDRONO, A. 2018 Numerical modeling of a granular collapse immersed in a viscous fluid. In *Advances in Hydroinformatics*, pp. 1099–1116. Springer.

KEMPE, TOBIAS & FRÖHLICH, JOCHEN 2012 An improved immersed boundary method with

direct forcing for the simulation of particle laden flows. *Journal of Computational Physics* **231** (9), 3663–3684.

Pierson, J.-L. & Magnaudet, J. 2018 Inertial settling of a sphere through an interface. part 2. sphere and tail dynamics. *J. Fluid Mech.* **835**, 808–851.

Yu, Z. & Shao, X. 2007 A direct-forcing fictitious domain method for particulate flows. *Journal of computational physics* **227** (1), 292–314.

Yuki, Y., Takeuchi, S. & Kajishima, T. 2007 Efficient immersed boundary method for strong interaction problem of arbitrary shape object with the self-induced flow. *Journal of Fluid Science and Technology* **2** (1), 1–11.